Proceedings of ASME Turbo Expo 2024
Turbomachinery Technical Conference and Exposition
GT2024
June 24-28, 2024, London, United Kingdom

GT2024-126791

NUMERICAL ANALYSIS OF A FLOW CONTROL SYSTEM FOR HIGH-PRESSURE TURBINE VANES SUBJECT TO HIGHLY OSCILLATING INFLOW CONDITIONS

Panagiotis Gallis [1], Simone Salvadori [1,*], Daniela A. Misul [1]

[1]Department of Energy (DENERG)
Politecnico di Torino
Corso Duca degli Abruzzi, 24
10129 – Torino, Italia

ABSTRACT

Under the prism of introducing pioneering technologies in the propulsive field, the Rotating Detonation Engine (RDE) continuously attracts the Gas Turbine (GT) research community. However, how to effectively couple an RDE with High-Pressure Turbine (HPT) stages is still debated. In fact, time-dependent flow conditions from the RDE greatly affect turbine performance, thus reducing the positive impact of Pressure Gain Combustion (PGC) on the overall cycle efficiency. The present numerical work aims at analysing both the impact of a pulsating inflow on the performance of a newly designed high-pressure turbine vane and the effectiveness of a flow control system in governing the oscillations within the vane passage. First, a baseline vane capable to ingest high enthalpy flow at an inlet Mach number of 0.6 is introduced. A total number of 297 samples are generated by varying the 18 geometrical parameters that characterize the vane's endwalls and airfoil profile with the help of Latin Hypercube sampling method. Then, an optimization strategy is performed using steady inflow conditions allows for minimizing vane's loss coefficient, thus providing the final geometry of the new vane. In the second part of the work, a flow control system is proposed by placing a series of holes in the endwalls of the vane. Air at constant stagnation conditions is injected upstream of vane's leading edge. Unsteady calculations with and without flow control, including similar pulsating conditions from the RDE provide an insight to the generation and evolution of the secondary flow structures inside of the passage. The main outcome of this analysis is that the flow control system intensifies the passage vortices providing less oscillating flow at the vane exit section, which is beneficial for the aerodynamic performance of a subsequent blade row.

Keywords: Pressure Gain Combustion, Rotating Detonation Engine, High–Pressure Turbine Vane, Computational Fluid Dynamics, Flow Control, Secondary Flows

*Corresponding author: simone.salvadori@polito.it

NOMENCLATURE

A	Area $[m^2]$
C	Chord $[m]$
Cp	Specific Heat Capacity $[J \cdot K^{-1} \cdot kg^{-1}]$
f	Frequency $[Hz]$
$\overline{DOE}$	Design of Experiments Matrix
o	Throat $[m]$
$\overline{P}$	Parametrized Sample
R	Gas Constant $[J \cdot K^{-1} \cdot kg^{-1}]$
T	Period $[s]$
s	Pitch $[m]$
t	Time $[s]$
T_t	Total Temperature $[K]$
u	Velocity $[m/s]$

Greek letters

α^o	Flow Angle $[deg]$
β	Inclination $[deg]$
$\delta\theta$	Pitch Distance $[deg]$
δx	Distance $[m]$
ξ	Rotating Angle $[deg]$
ρ	Density $[kg \cdot m^{-3}]$
σ	Entropy Per Unit Mass $[J \cdot K^{-1} \cdot kg^{-1}]$

Dimensionless groups

$\hat{C}$	Cross-Correlation Coefficient $[-]$
CR	Contraction Ratio $[-]$
D	Damping Factor $[-]$
GCI	Grid Convergence Index $[-]$
Ma	Mach Number $[-]$
M	Blowing Ratio $[-]$
Y	Total Pressure Loss Coefficient $[-]$
Y_{cl}	Clearance Loss Coefficient $[-]$

Y_{ex} Supersonic Expansion Loss Coefficient [−]
Y_{lw} Lashing Wire Loss Coefficient [−]
Y_p Profile Loss Coefficient [−]
Y_s Secondary Flow Loss Coefficient [−]
Y_{te} Trailing Edge Loss Coefficient [−]
Y_{sh} Shock Loss Coefficient [−]
ζ_{α^o} Flow Angle Deviation Coefficient [−]
ζ_{P_t} Total Pressure Losses [−]
ζ_v Loss Coefficient [−]
η Efficiency [−]
ϕ Massflow Ratio [−]

Superscripts and subscripts

$\hat{}$ Reduced
CA Cycle Average
$ax.$ Axial
ex Outlet
in Inlet
inc Incidence
$is.$ Isentropic
MA Mass-Weighted Average
M Mach
m Mixing
$P,\ p$ Profile
RE Reynolds
s Secondary Flows
sh Shock
te Trailing Edge
WP Weighted-Pressure Mixed Efficiency
t Total
WA Work Average

Acronyms

BC Boundary Conditions
DOE Design of Experiments
GT Gas Turbine
HDB Hub Diffusive Bubble
HPT High-Pressure Turbine
HPV Hub Passage Vortex
IGV Inlet Guide Vanes
NLPQL Non-Linear Programming by Quadratic Lagrangian
PDE Pulse Detonation Engine
PGC Pressure Gain Combustors
RANS Reynolds–Averaged Navier–Stokes
RDE Rotating Detonation Engine
TDB Tip Diffusive Bubble
TPV Tip Passage Vortex
URANS Unsteady Reynolds–Averaged Navier–Stokes

1. INTRODUCTION

In the context of designing more sustainable propulsion systems, the current efforts of the Gas Turbine (GT) research community are concentrated on the re–evaluation of the ensemble GT architecture. Inevitably, the conventional burners are under investigation because their quasi iso–baric combustion process induces considerable pressure losses on the cycle. One of the solutions that is under investigation are the Pressure Gain Combustion (PGC) cycles [1]. PGC cycles are characterised by the alternative combustion modes of detonation or iso–choric deflagration, which are able to rise the stagnation flow properties during the exothermic process [2]. As a result, these alternative combustors can offer higher inlet temperature for the subsequent expansion system. Hence, their theoretical cycle efficiency is larger than the conventional Joule–Brayton cycle [3, 4].

One of the most promising PGC machine is the Rotating Detonation Engine (RDE) [5, 6]. This combustor is consisted of two co–axial cylinders which provide an annular chamber [7]. Fuel and air are inserted inside of the chamber and, with the help of a pre–detonator tube or a spark plug ignitor a detonation wave is formed. The wave spins around the annulus while its frequency achieves the order of $1 - 10\ kHz$. The advantages of the RDE in a GT cycle were investigated in details by Sousa *et al.* [8]. In particular, a 1D thermodynamic cycle code provided a comparison of the performance between a GT that utilized a conventional burner with a machine that functioned with an RDE. They demonstrated that the benefit of RDE was especially profound at low overall pressure ratios which led to less weight and specific fuel consumption. Nevertheless, these benefits should not be counteracted by the harsh outflow of this machine. RDE's exhaust is characterized by a spatial–temporal variation of the stagnation pressure, stagnation temperature and flow angle [9–11]. These strong variations impact on the proper function of the High-Pressure Turbine (HPT) stage. Therefore, it is important to ensure that the turbine's efficiency deficit would not counteract the benefits of the RDE's performance.

In spite of the obvious challenges on the experimental analysis of RDE–axial turbine interactions, there were conducted important research works on this field. Naples *et al.* [12] replaced the combustion core of T63 (C20–250) gas turbine adding a RDE, they monitored the turbine's efficiency and underlined that high frequency unsteadiness by RDE did not deteriorate significantly the turbine's performance. Zhou *et al.* [13] underlined the importance of the RDE's oblique shock reflection on the following turbine Inlet Guide Vanes (IGVs). In particular, Wei *et al.* [14] showed that when the oblique shock propagation was tangent (misaligned) to axial chord of IGVs and not normal (aligned), the reflection was more chaotic and complex. Furthermore, Wu *et al.* [15] proved that the misaligned cases attenuated more the flow field in terms of pressure. Bach et al. [16] conducted several experiments of an RDE coupled with IGVs of NACA 0006 profile of which the stagger angle was variable. They concluded that the detonation wave preferred the alignment case because probably less reflected shocks were being guided back to RDE while this configuration was more able to start the passages of IGVs.

In parallel, several numerical activities have being conducted recently. Concerning inlet supersonic flow, Paniagua *et al.* [17] designed a supersonic turbine able to ingest the high enthalpy flow by an RDE and analysed the peculiar flow field during the starting phase. Moreover, Liu *et al.* [11] analysed with transient CFD simulations the performance of a supersonic turbine stage under the influence of rotating oblique shock of variable amplitude and frequency. Asli *et al.* [18] tested numerically the NACA 0006 vane under different solidity and area reduction. They concluded that by increasing solidity or thickness–to–chord ratio, the total pressure loss coefficient decreased. In parallel, velocity angle attenuation increased. For the case of the transonic vanes, Liu *et*

al. [19] modified the endwalls of the vane in order to keep the contraction ratio below the isentropic limit and they numerically analysed a conventional HPT stage with inlet Mach number of 0.3 and 0.6 under axial uniform pulsation. They highlighted the creation of a separation bubble in the diffusive modified vane endwalls. Further CFD analysis [20] uncovered that inlet Mach of 0.3 offered better stage efficiency, whereas higher attenuation is achieved with inlet Mach number of 0.6. Furthermore, steady and unsteady optimization process of the hub and tip contouring [21] assessing the damping and losses emphasised the importance of the stage's endwalls. Later, a multi-point optimization strategy with CFD analysis by Grasa *et al.* [22] was focused on the reduction of total pressure losses and the homogeneity of vane's outflow to prevent blade's forcing.

The topic of the current manuscript is the design of a vane able to ingest the high enthalpy flow by an RDE and a proposal of a flow control system to attenuate the incoming oscillations. First, the straight hub and tip endwalls of the CT3 vane are modified and parameterized resulting in an area ratio favourable to offer inlet Mach number around 0.6. Simultaneously, the vane's airfoil is parameterized as well. A Design of Experiments (DOE) using the Latin Hypercube sample method is created. Steady CFD analysis is performed for every sample and an optimization methodology provides a vane with the minimum loss coefficient. In the second part of this work, a flow control system is proposed. At tip and hub, a series of tubes upstream of the leading edge are placed to inject cooled steady air to the endwalls region of the vane. In parallel, the main incoming flow is subjected to fluctuation of total pressure, total temperature and flow angle of various frequencies. The vane with and without the flow control system is tested numerically using transient simulations. In the end, the peculiar motion of the secondary flows is thoroughly discussed and the advantages of the flow control system are underlined.

2. VANE OPTIMIZATION

In this part the design of a vane with diffusive endwalls is presented. In Section 2.1, the parametrization of the vane's geometry is introduced, the resulting DOE is presented and the elected optimization strategy is highlighted. Section 2.2 provides information of the numerical configuration of the steady CFD calculations of every sample. In the end, the results of the optimization method and the flow field comparison of the baseline and optimized geometry are discussed in Section 2.3.

2.1 DOE and Optimization Strategy

The optimization method serves as a starting point of the transient analysis of a subsonic HPT vane under varying inlet boundary conditions. Before proceeding in the unsteady evaluation, it is necessary to provide a benchmark case. The vane that serves as baseline for the optimization method is the CT3 vane [23]. This profile is selected because it suits the characteristics of a typical HPT vane. The first modification is the axisymmetric diffusive tip and hub endwalls upstream of the leading edge. In parallel, the airfoil profile is parametrized as well. Thus, the first part of this manuscript focuses on the optimal combination of endwalls and stator's airfoil that generates the lowest amount of losses. In Table 1, the information of vane samples is introduced.

TABLE 1: GEOMETRICAL FEATURES OF DOE

C	75.7 $[mm]$
$\mathbf{N_{Vanes}}$	43 $[-]$
$\mathbf{R_{Shaft}}$	369.85 $[mm]$
$\mathbf{DR_{Inlet}}$	8.6 $[mm]$
$\mathbf{DR_{Outlet}}$	25.35 $[mm]$

The chord value (C) is referred to baseline case of CT3 vane. The term DR_{Inlet} is referred to the radial distance by the shaft radius which must be subtracted or added for the construction of inlet hub or tip respectively. Similarly, DR_{Outlet} governs the creation of the downstream tip and hub part of the vanes.

In Fig.1a, the parametrization of the meridional profile is portrayed. The straight inlet channel is substituted by an opening inlet section. The reason behind this choice emerges from the reduction of the contraction ratio to help the vane to ingest the high enthalpy flow by an RDE. This design selection came after the consideration of a numerical work [20] that stressed the advantages of this option. The hub and tip endwalls are identically created using b-splines of 8 control points. Due to the radial equilibrium, the flow field will not be axisymmetric inside the passage. Nonetheless, the design selection of axisymmetric endwalls is elected to not increase the number of parameters and consequently the numerical cost of the optimization process. In particular only 4 control points are variable with one degree of freedom (DOF) in the $z-$axis. Starting from the inlet, the radial position of the first two control points is elected to serve an inlet Mach number of 0.6 by providing an appropriate area ratio between the inlet cross–section area and the nominal throat area of CT3 vane for the baseline case. On the other hand, the radial position of the third point is elected to be 19 % below of the downstream straight tip fixed control points. It is preferred the modified endwalls to affect a small part of the span. In addition, the radial position of the 4^{th} control point is elected to be in the middle distance between the 3^{rd} control point and the final tip position of the stator.

In parallel, the airfoil profile is constructed by 2 b-splines for the pressure and suction side (Fig.1b). For this purpose, 12 control points are used, while only 8 of them are free to vary. Moreover, the stagger angle of geometry is added as an another geometrical variable parameter. The choice of only 2D airfoil profile parametrization and not the inclusion of bow, lean and sweep is taken in order to not increase the number of the parameters and the numerical cost of the optimization. In fact, the stacking law of the vane profile can be explored after defining the optimum endwalls and airfoil profile in a future advanced optimization study. In total, a sample can be reconstructed with 18 parameters. In Fig.1c and Fig.1d the baseline geometry is depicted with red colour. The DOE is created with the help of Latin Hypercube sampling method. By modifying appropriately the variable control points of Fig.1a and Fig.1b, 297 geometries are produced. Since this is the first optimization of the current specific case, the number of DOE is elected as an estimation of the needs of the analysis. In Fig.1c and Fig.1d the samples of

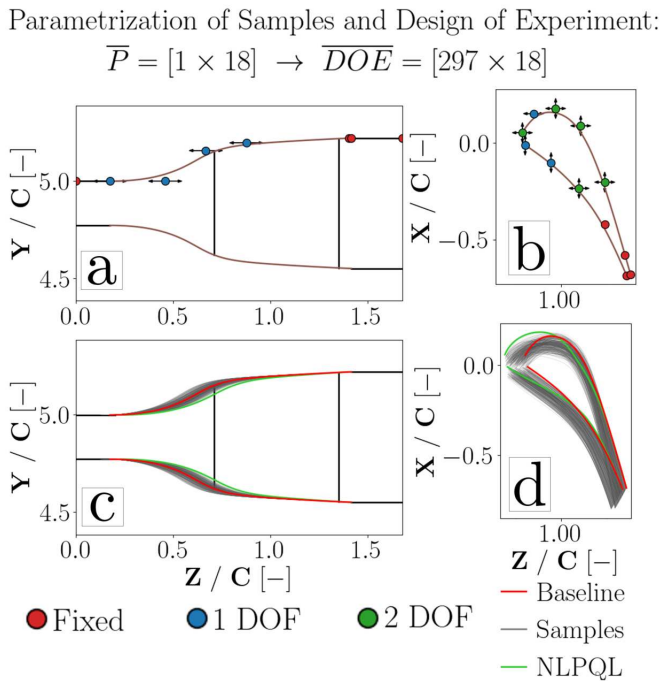

FIGURE 1: PARAMETRIZATION OF VANE'S GEOMETRY AND DOE

DOE are coloured with grey scale.

The single–objective optimization process is conducted with the help of ANSYS DesignXplorer tool. After completing the parametrization and the DOE of the samples, each cases is tested numerically with the help of ANSYS CFX solver. The validation of the solver is provided in Appendix A. The steady Reynolds–Averaged Navier–Stokes (RANS) equations are solved for each sample for the nominal boundary conditions of CT3 vane. For every sample, the loss coefficient of Eq. 1 is computed by monitoring the conditions between the inlet (1) and outlet (2) of the vane.

$$\zeta_v = 1 - \frac{1 - \left(\frac{P_2}{P_{t,\,2}}\right)^{\frac{\gamma-1}{\gamma}}}{1 - \left(\frac{P_2}{P_{t,\,1}}\right)^{\frac{\gamma-1}{\gamma}}} = 1 - \frac{u_2^2}{u_{2,\,is.}^2} \tag{1}$$

Once each sample is numerically assessed, the Genetic Aggregation (GA) method is used to interpolate and construct a response surface. Afterwards, the optimization of the response surface takes place. With the use of Non-Linear Programming by Quadratic Lagrangian (NLPQL) method, three new individuals are constructed. Later, the three new samples are numerically tested and the best candidate is chosen. Thus, the optimization occurs for only one round of three individuals. The optimization methodology is inspired by the work of Ayancik *et al.* [24] which tested different meta–models for the design optimization of Francis type turbine runners.

Despite the fact the loss coefficient is the only objective function of the optimization algorithm, other two properties are calculated for each case. Another evaluation metric is the outlet deviation coefficient of Eq. 2. This property compares the deviation of the outlet flow angle with respect the outlet metal angle of

ht]

	Grid	Refinement Ratio	GCI	Asymptotic Range of Convergence
$(\dot{m})_{\text{Inlet}}$	C–M	1.2587	1.4107 %	1.029
	M–F	1.2494	0.92348 %	
$(Ma)_{\text{Inlet}}$	C–M	1.2587	1.9418 %	1.032
	M–F	1.2494	1.2732 %	
$(P_t)_{\text{Out}}^{\text{Vane}}$	C–M	1.2587	0.064 %	1.064
	M–F	1.2494	0.0224 %	

TABLE 2: GRID DEPENDENCY ANALYSIS FOR DOE SAMPLES

the nominal CT3 vane which matches with the inlet metal angle of the subsequent CT3 blade. In addition, it is important to stress that the parametrization of the vane imposes a variable throat area for each sample, as the airfoil and endwalls shape are significantly varying. On the other hand, the inlet area of each vane remains the same. Therefore, the contraction ratio of each geometry is computed in accordance to Eq. 3.

$$\zeta_{\alpha^o} = 1 - \frac{\alpha_2^o}{\alpha_{2,\,metal}^o} \tag{2}$$

$$CR = \frac{A_{Inlet}}{A_{Throat}} \tag{3}$$

2.2 Numerical Setup of DOE

After the definition of the DOE, each sample volume is meshed and the boundary conditions are inserted. In Fig. 2, different views of the baseline grid are displayed. The colours of Fig. 2a and Fig. 2b are in accordance to the boundary conditions of Table. 3. The properties that are used for meshing each sample are elected after performing the grid dependency analysis of the baseline case. Three mesh volumes are tested by the solver using the boundary conditions of Table. 3. For the baseline case, a coarse grid (981327 elements), a medium grid (1956968 elements) and a fine grid (3816709 elements) are constructed. The flow properties that are used for the purposes of the analysis are the mass flow rate and mass–weighted Mach number at the inlet of the domain. In addition, the mass-weighted stagnation pressure at the outlet of the vane is assessed for each meshed volume. For a flow property (Φ), the mass–weighted average value of a specific location is given by Eq. 4.

$$\Phi^{MA} = \frac{\int_A \rho u \Phi \, dA}{\int_A \rho u \, dA} \tag{4}$$

The Grid Convergence Index (GCI) is calculated as indicated by the grid dependency analysis by Roaches *et al.* [25]. The results are placed at Table 2. For each flow property GCI decreases, while the asymptotic range of convergence is very close to 1. Consequently, the mesh properties of the medium grid can be used for each sample as they provide grid independent results for the baseline case.

Once the boundary conditions are defined, the steady Reynolds–Averaged Navier–Stokes (RANS) equations are solved for each geometry. The commercial software Ansys CFX, which

Boundary Conditions	
Type	Properties
Inlet	$P_t = 161600\ [Pa]$ & $T_t = 440\ [K]$
Outlet	$P = 83289\ [Pa]$
Periodic	-
No–Slip Wall	Adiabatic

TABLE 3: BOUNDARY CONDITIONS OF SAMPLES

implements a pressure-based implicit coupled solver, is used for this purpose. A high-resolution scheme is selected for the advection terms and the turbulence, while the k–ω SST model [26] is selected for turbulence closure. Furthermore, an inflation layer is placed close to the viscous walls of each sample to ensure that the y^+ is maintained below 1 for proper boundary layer resolution. The working fluid is air, which is assumed to be ideal gas.

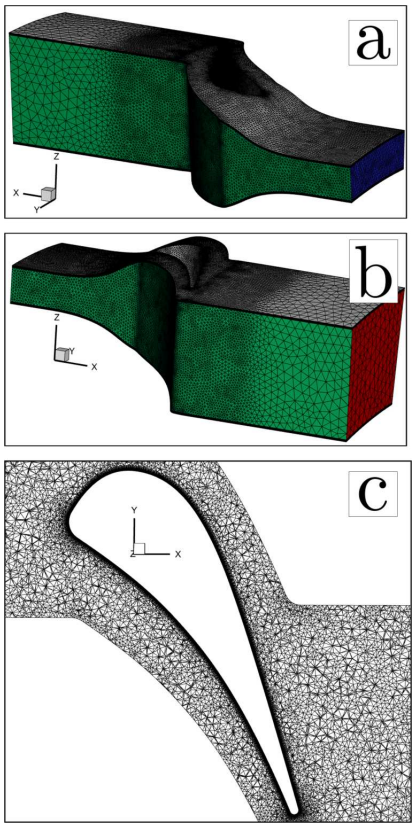

FIGURE 2: MESH OF DOE SAMPLES

2.3 DOE Results

In Fig. 3 the results of the DOE are introduced. The $x-$axis is expressed with the help of outlet deviation coefficient Eq. 2, while the $y-$axis is the loss coefficient of Eq. 1. In parallel, every sample is coloured with its contraction ratio value of Eq. 3. All samples are subjected to the same boundary conditions. Hence, all the cases are characterised by the same pressure ratio and inlet total temperature. Nonetheless, it is already mentioned that each case results in different contraction ratio value. The inlet cross–section area is the same for every sample, therefore each tested geometry provides different minimum area to the flow field. Therefore, different throat area of each case results in different mass flow rate. In addition, a Pareto front can be identified for the analysed cases. The baseline configuration is placed with a different symbol. The provided geometry by the optimization of the response surface using the NLPQL method is highlighted as well. As it can be seen, the optimized solution is away of the barycentre of the samples. Therefore, the design space should be explored more in the DOE phase. Although, with a limited number of cases, NLPQL method provides a very improved solution. The shape of the NLPQL geometry is displayed with green color in Fig. 1c and Fig. 1d. The geometrical data of the diffusive endwalls and vane airfoil are included in Appendix C. The optimization process is able to offer a sample, which keeps the losses below of 10 %, while its deviation by the prescribed outlet metal angle is less than 2 %.

It is evident that if a sample is characterised by high contraction ratio, the losses are significantly increased. This conclusion agrees with the trend of a similar optimization process [22]. First of all, the pressure ratio of each sample is below the critical one providing samples in the transonic regime. For the worst case the contraction ratio is high (2.22) and the inlet Mach number is relatively low (0.27). Therefore, the losses are quite high and the goal of inlet Mach number close to 0.6 failed. On the contrary, the low contraction ratio of the best case (1.21) offers the minimum loss coefficient with an inlet Mach number close to the target of the analysis (0.575).

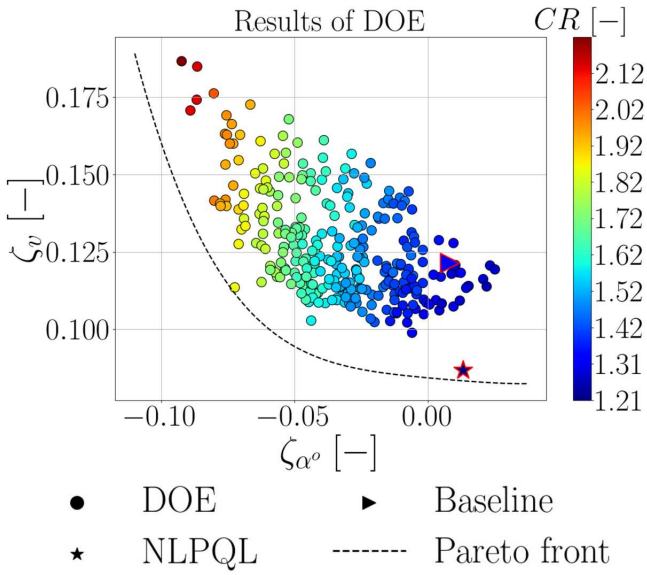

FIGURE 3: RESULTS OF DOE

A flow field comparison of the baseline and optimized geometry is necessary to investigate the reasons behind the superiority of the NLPQL design. Under that prism, the vorticity magnitude serves as an indicator of the secondary flow footprints. In Fig. 4a and Fig. 4b views from leading and trailing edge of the baseline geometry are displayed respectively. The onset of passage vortex

close to the suction side of the leading edge can be identified. In particular, the size of this vortex is enlarged as the incoming horseshoe vortex is affected by the creation of the diffusive bubble. This zone of separation is triggered by the diffusive endwalls in the tip and hub of the vane. As a consequence, the horseshoe vortex meets the diffusive bubble, enlarges its size and forms an intensified passage vortex. This flow structure propagates close to the suction side of the channel due to the low pressure level of that side. This evolution can be seen in the tip region where the tip passage vortex (TPV) and the tip diffusive bubble (TDB) are illustrated. Similarly, the hub passage vortex (HPV) and hub diffusive bubble (HDB) are indicated. In the end, the outflow of baseline sample is covered by an extensive zone of TPV and HPV in Fig. 4b.

In the same way, the vorticity magnitude shed the light on the secondary flows evolution of the optimized geometry in Fig. 4c and Fig. 4d. The region and the intensity of the diffusive bubbles and the passage vortices are significantly reduced. As a result, the outflow of the optimized geometry offers a flow field with TPV and HPV of smaller size and strength while their zones are restricted closer to the endwalls. Hence, the profound benefits in terms of loss coefficient of the optimized case can be justified by the less energetic secondary flows. Nonetheless, even the optimized design delivers an accelerated flow field where the TPV and HPV are larger comparing to a conventional HPT vane with straight endwalls. If the inflow of the vane is significantly perturbed, as in the case of RDE, these vortical structures will oscillate and will be guided inside the subsequent blade. Hence, the deterioration of the stage efficiency will not solely take place due to the unsteady flow field. The enlarged TPV and HPV will oscillate even more and they will worsen the blade's performance. Thus, it is necessary to investigate an appropriate flow control system, which will manage to control the secondary flows motion.

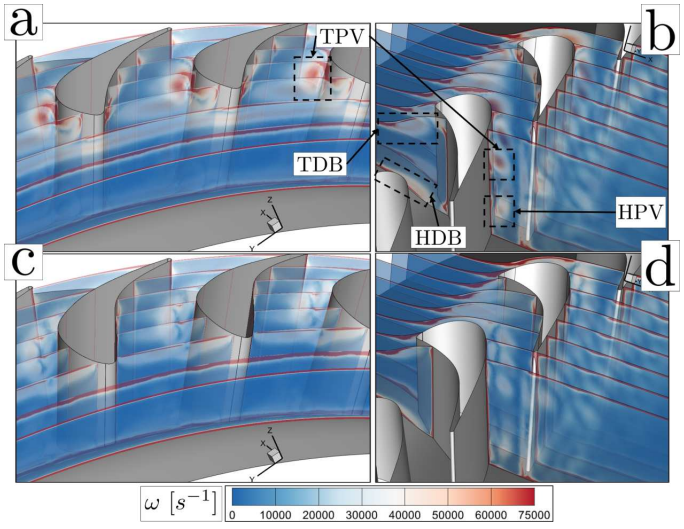

FIGURE 4: COMPARISON OF SECONDARY FLOW STRUCTURES OF BASELINE (a & b) AND OPTIMIZED GEOMETRY (c & d)

3. FLOW CONTROL SYSTEM

In this part the flow control analysis is presented. In Section 3.1, the flow control concept is introduced. Section 3.2 includes the numerical set up of the simulations, while in section 3.3 the evaluation of a vane under pulsation and cooling supply is illustrated. In the end, the results of the flow control analysis are discussed in Section 3.4.

3.1 Flow Control Concept

In Fig. 5, the flow control system is portrayed. The transonic vane with the diffusive endwalls provided by the optimization process is used in this case. Upstream of the leading edge, a series of tubes are inserted in the hub and the tip of the vane. The idea behind this conceptual design is to supply additional air in the region of the developed secondary flows. Therefore, it will be more difficult for a pulsating inflow to extensively perturb the re–enforced passage vortex. As a consequence, the vortical structures at the outlet of the vane will oscillate less leading to a more uniform flow for the subsequent rotor.

In Fig. 5, the parametrization of the flow control system can be identified. A single series of tubes is utilized at the tip and hub respectively. It should be noted that the tubes are placed equally in the pitch-wise direction. By controlling the pitch of the first tube with respect the leading edge ($\delta\theta$), the pitch distance of the tubes varies accordingly. In particular, the inclination with respect of the diffusive endwalls (β), the leading edge distance (δx), the rotating angle (ξ) and the pitch of the first tube with respect the leading edge are fixed as it can be observed in Fig. 5. As a result, the blowing orientation in the meridional plane (β) is completely axial without imposing any additional radial momentum component to the flow field (Fig. 5a). In parallel, the orientation of the tubes in the blade-to-blade view (ξ) at the tip (Fig. 5b) is chosen as an approximation of the theoretical streamlines upstream of the passage. The scope of the current activity is to investigate the influence of the flow control at the endwalls of the diffusive vane under pulsation and not the role of the aforementioned geometrical features. Hence, a first guess of the geometrical properties is conducted aiming at solely contribute to the formation of the secondary flow structures. The values of the current flow control case can be found in Table 4. It must be underlined that in the table the reported value of β is assessed with respect the axis–x and not the tangent to the endwalls, as indicated Fig. 5a.

TABLE 4: GEOMETRICAL FEATURES OF FLOW CONTROL

β	0 $[deg]$
δx	4.31 % of C
ξ_1	8 $[deg]$
ξ_2	−20 $[deg]$
ξ_3	−7.5 $[deg]$
ξ_4	0 $[deg]$
ξ_5	5 $[deg]$
$\delta\theta$	20 % of pitch
d_{hole}	1.98 % of C

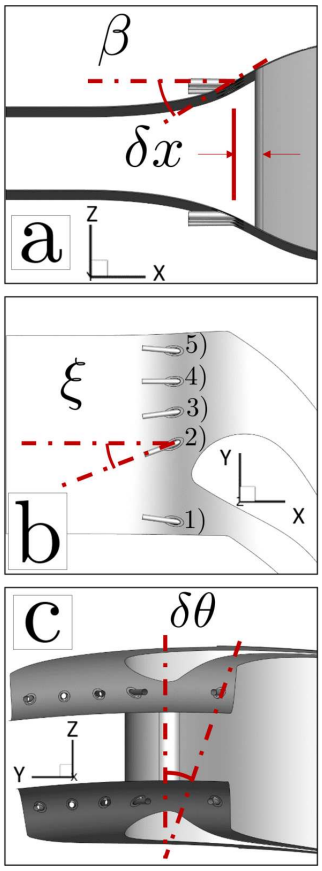

FIGURE 5: FLOW CONTROL CONCEPT

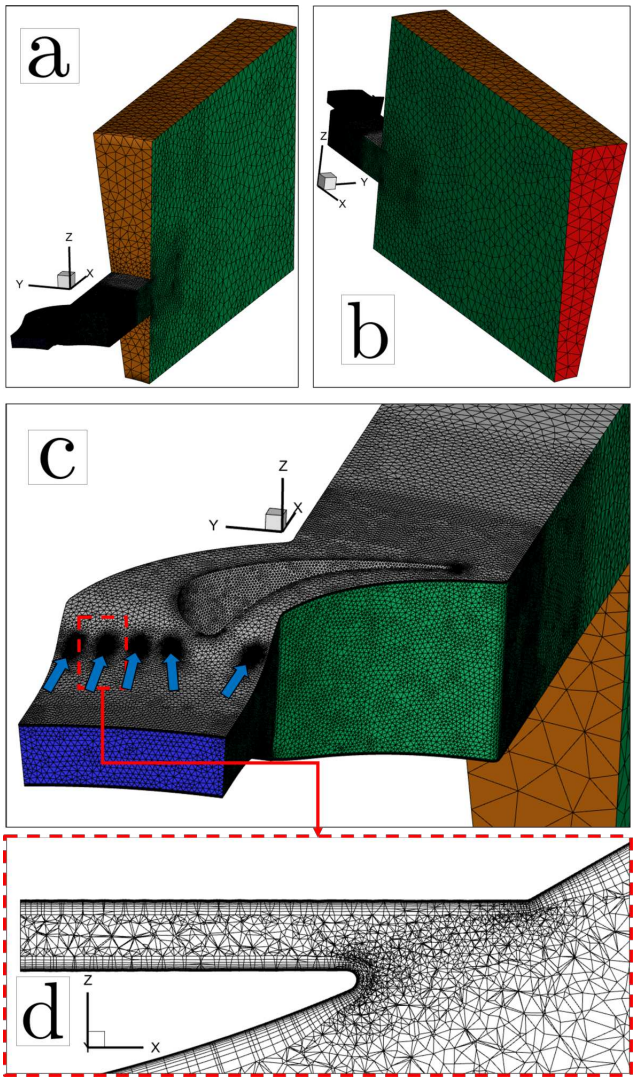

FIGURE 6: GRID OF FLOW CONTROL DOMAIN

3.2 Numerical Setup

The goal of the analysis is the comparison of the vane performance with and without the flow control system under oscillating boundary conditions. In Fig. 6, the flow domain of the vane with the flow control system is depicted. In Fig. 6a and Fig. 6b it can be observed a large plenum at the aft part of the vane. This large coarse volume serves as a damper of the pulsating flow field focusing on the prevention of spurious pressure waves to be reflected by the outlet boundary [27]. Fig. 6c offers a view of the flow control vane domain, while Fig. 6d concentrates on the cross section of the meshed volume in the tube region. As it can be seen, an inflation layer is placed close to the viscous wall in order to resolve the boundary layer by preserving the y^+ values below one. The colours of the boundary faces of Fig. 6 are in accordance with the Table 5. For the flow control case the grid size is 3782392 elements. The configuration of the flow volume with the artificial plenum, the mesh properties and the boundary conditions are identical for the case without the flow control system resulting in a grid size of $\approx 2.1 \cdot 10^6$ elements.

The harsh outlet flow field of the RDE incommodes any detailed accurate experimental investigation of the exhaust field properties. At the outlet of RDE, the stagnation pressure, temperature flow angle follow a spatio–temporal variation [28, 29]. In the current study, the spatial extension of this variation is omitted. The inflow exhibits only a temporal evolution of the aforementioned flow properties. In Fig. 7, the utilized pulsating inlet boundary conditions of the system are introduced. In particular, their morphology is inspired by a numerical work focusing on the outlet nozzle configuration of an RDE [30]. Nonetheless, the analysis attempts to explore the influence of the control system in a preliminary stage. Hence, the boundary conditions are scaled down to provide time average values equal to the operating point of the nominal CT3 stage ($\overline{P_t}$ = 161600 Pa, $\overline{T_t}$ = 440 K & $\overline{\alpha}$ = 0 deg). Concerning the flow control system case, the vane is tested under different blowing conditions. In fact, the supplying stagnation temperature is kept constant, while the influence of the stagnation pressure is investigated. F.C.1 introduces a case in which the blowing pressure is smaller than the minimum pulsating pressure. F.C.2 is an analysis in which the blowing pressure is equal to the minimum pulsating pressure, while F.C.3 provides a blowing pressure equal to the maximum pulsating pressure. It must be stressed that the inlet boundary conditions of the main flow result in oscillating static pressure at the region of leading edge and at the entrance of the vane's passage. Thus, if ones concentrates to the flow

Boundary Conditions	
Type	Properties
Inlet	$P_t = f(t)$, $T_t = f(t)$ & $\alpha = f(t)$
Outlet	$P = 83289\ [Pa]$
Periodic	-
Free–Slip Wall	Adiabatic
No–Slip Wall	Adiabatic

TABLE 5: BOUNDARY CONDITIONS OF FLOW CONTROL VOLUME

TABLE 6: FLOW CONTROL CONDITIONS

Case	P_{tb}	T_{tb}
w/o F.C.	-	-
F.C.1	153311.5 [Pa]	300 [K]
F.C.2	160812.03 [Pa]	300 [K]
F.C.3	162841.5 [Pa]	300 [K]

control tubes and considers them as single control volumes, their back pressure varies in time. Consequently, if the supplying total pressure is less than the maximum value of the oscillating static pressure at these specific locations, the main flow will enter inside the flow control tubes. This scenario is avoided by calculating with the help of isentropic equations the resulting static pressure at the entrance of the passage for each time moment without flow control system. Thus, the flow control conditions are chosen accordingly to avoid any case of reverse flow. This choice should be considered for the future investigation of the flow control system with realistic boundary conditions by the RDE. In Table 6, the three different cases of the flow control analysis are placed.

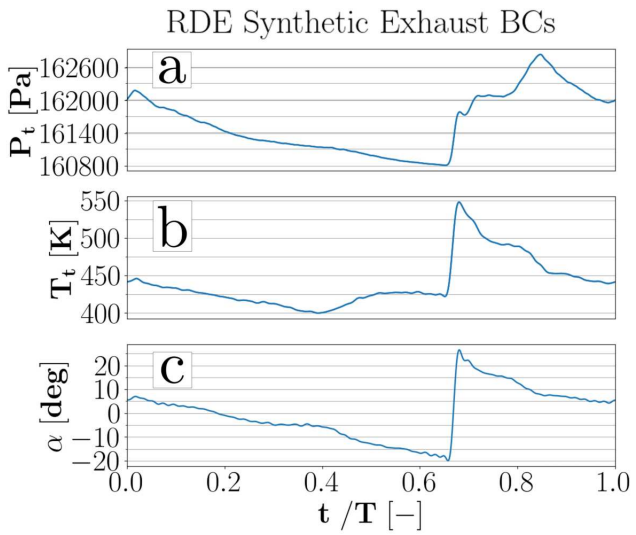

FIGURE 7: PULSATING BOUNDARY CONDITIONS

The meshing properties are derived by a grid dependency analysis. Similarly with Section 2.2, the Grid Convergence Index (GCI) [25] is calculated for a coarse (2524299 elements), medium (3782392) and fine mesh (5348320 elements) of the flow control case. The medium grid is identical to the meshed volume that is used for the flow control analysis. The results are placed at Table 7. Apart of the inlet mass flow, inlet mass–weighted Mach number and outlet mass–weighted total pressure, the blowing ratio between the purging tubes and the main flow is computed for the three cases. The blowing ratio compares the product of density with velocity of the flow control tubes with the same product of the main flow. The calculation is given by Eq 5. The mass flow rate over the flow cross–section area of each tube hole is compared with the mass–weighted density and velocity at the inlet of the vane (Fig. 8). For the purposes of grid dependency analysis, the boundary conditions at the vane's inlet correspond to initial time moment of Fig. 7, while F.C.1 is used for the inlet of the flow control tubes. For each flow property GCI decreases, while the asymptotic range of convergence approaches 1. Consequently, the results of flow control analysis are grid independent.

$$M = \frac{u_b \cdot \rho_b}{u_{main} \cdot \rho_{main}} = \frac{\Sigma_{i=1}^{10} \dot{m}_i \ / \ \Sigma_{i=1}^{10} A_i}{u_{01}^{MA} \cdot \rho_{01}^{MA}} \tag{5}$$

	Grid	Refinement Ratio	GCI	Asymptotic Range of Convergence
$(\dot{\mathbf{m}})_{\text{Inlet}}$	C–M	1.1443	0.0273 %	1.043
	M–F	1.1430	0.0014 %	
$(\mathbf{Ma})_{\text{Inlet}}$	C–M	1.1443	0.0676 %	1.04
	M–F	1.1430	0.0053 %	
$(\mathbf{P_t})_{\text{Out}}^{\text{Vane}}$	C–M	1.1443	0.1466 %	1.015
	M–F	1.1430	0.0299 %	
M	C–M	1.1443	0.0459 %	1.027
	M–F	1.1430	0.004 %	

TABLE 7: GRID DEPENDENCY ANALYSIS FOR FLOW CONTROL ANALYSIS

The vane with and without flow control system is analysed under the pulsation of four different frequencies. The investigated periods result in 0.5 kHz, 1 kHz, 2.5 kHz and 5 kHz. In Table 8, the pulsating frequencies are expressed as reduced frequencies, in accordance to Eq. 6. Reduced frequency provides the information of how fast a pulsation varies by comparing the convective time that the oscillation needs to pass the domain of interest. In particular, if the reduced frequency is below the unity, the pulsation varies slower than it convects. On the other hand, if the reduced frequency exceeds the unity, the oscillation perturbs faster than it convects. The current analysis investigates a sufficient range of reduced frequencies.

$$\hat{f} = \frac{f_{pulsation}}{\overline{u}_{in} \ / \ c_{ax.}} \tag{6}$$

The Unsteady Reynolds–Averaged Navier–Stokes (URANS) equations are solved using a fully 2^{nd} order accurate density—based implicit solver of ANSYS FLUENT. Turbulence is calculated with help of k–ω SST turbulence model [26]. The frequency of the analysis is 100 times higher than the pulsating frequency of each case ensuring the proper resolution of the oscillations. It is necessary to define a criteria for the periodic (unsteady) convergence of the flow domain through the analysis. For this reason,

TABLE 8: ANALYSED FREQUENCIES OF PULSATION

f	0.5 $[kHz]$	1 $[kHz]$	2.5 $[kHz]$	5 $[kHz]$
$\hat{f}$	0.227 $[-]$	0.454 $[-]$	1.138 $[-]$	2.275 $[-]$

the mass flow, mass–weighted average Mach number and mass–weighted average total temperature of the locations indicated in Fig. 8 are calculated.

Once the aforementioned properties are monitored in time, the cross–correlation is performed between two sequential cycles for each property. As a result, the minimum, average and maximum values of cross–correlation for zero lag for the same properties in various locations can be deduced. For the case without flow control for 5 Hz, the values are displayed in Fig. 9. The graphs demonstrate that in the eight cycle the periodicity is established throughout the whole flow domain of interest. This analysis is performed for every frequency with and without flow control ensuring that the eight resolved cycle can offer representative results.

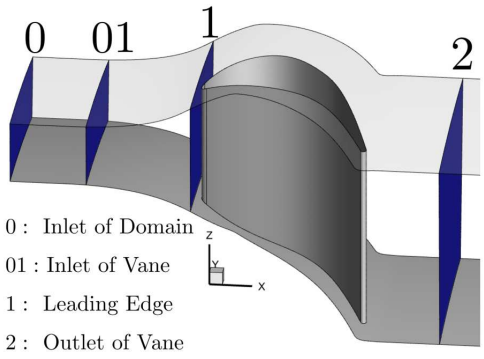

FIGURE 8: SAMPLING LOCATIONS

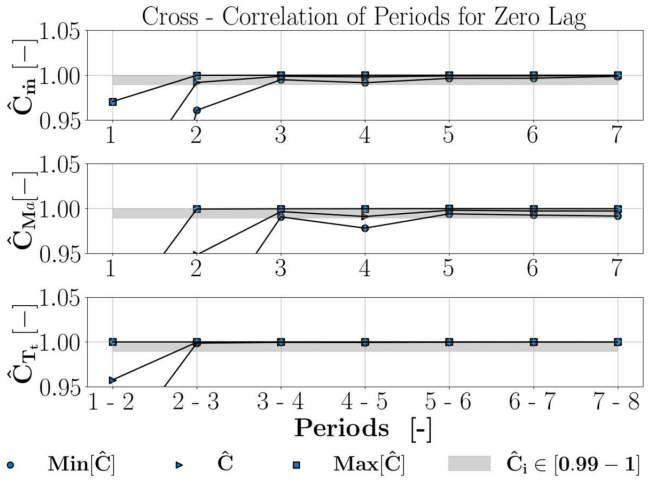

FIGURE 9: UNSTEADY PERIODIC CONVERGENCE VIA CROSS–CORRELATION

3.3 Evaluation of Vane

The current analysis imposes two main difficulties on assessing the vane's performance. The first issue emerges from the pulsating nature of the flow field. An instantaneous calculation of the stator's efficiency would lead to time moments when the inlet stagnation pressure is less than the outlet. Hence, the efficiency would exceed the unity. In order to avoid this problem, the cycle average approach of the flow properties is applied. Cumpsty *et al.* [31] suggested that the extensive properties and total temperature can be mass–weighted averaged, as in Eq. 4. As a result, the cycle average of a mass–weighted average property is retrieved by Eq. 7. This approach is applied on the stagnation temperature, velocity and flow angle for the pulsating analysis. On the contrary, the stagnation pressure for turbomachinery applications [32–34] follows the approach of work averaging of Eq. 8.

$$\overline{(\Phi)}^{MA} = \frac{\int_0^\tau (\Phi)^{MA} \cdot \int_A \rho u \, dA \, dt}{\int_0^\tau \int_A \rho u \, dA \, dt} \tag{7}$$

$$\overline{(P_t)}^{WA} = \left[\frac{\int_0^\tau \int_A \rho u T_t \, dA \, dt}{\int_0^\tau \int_A \rho u \left[\frac{T_t}{(P_t)^{\frac{\gamma-1}{\gamma}}}\right] dA \, dt}\right]^{\frac{\gamma}{\gamma-1}} \tag{8}$$

Therefore, the cycle average values of stagnation properties at inlet and outlet are now defined. Nevertheless, the static pressure at the outlet of vane oscillates in time as well. One approach can be the time average of area average static pressure of Eq. 9.

$$\overline{(P)}^{AA} = \frac{1}{\tau \, A} \int_0^\tau \int_A P \, dA \, dt \tag{9}$$

Consequently, for an unsteady inflow all the properties related to vanes performance are defined. In this part of the analysis, the loss coefficient will be expressed as stator efficiency following the approach of Young *et al.* [35]. The cycle average stator's efficiency and cycle average deviation coefficient are presented in Eq. 10 and Eq. 11 respectively.

$$(\overline{\eta})_v^{CA} = \frac{(\overline{u}_2^{CA})^2}{(\overline{u}_{2,\,is.}^{CA})^2} \tag{10}$$

$$(\overline{\zeta})_{\alpha^o}^{CA} = 1 - \frac{(\overline{\alpha_2^o})^{MA}}{\alpha^o_{2,\,metal}} \tag{11}$$

The second issue to this analysis concerns the flow control. If the aforementioned efficiency definition is followed, the influence of the cooling supplied air will be omitted. Hence, it should be found a definition in which the cooling air is included in the analysis. Young *et al.* [35] proposed the Weighted-Pressure (WP) Mixed Efficiency of Eq. 12.

$$(\eta)_{WP} = \frac{h_{t2} - h_2}{h_{tw} - h_{2,\,isw}} = \frac{1 - (\frac{T_2}{T_{t,\,2}})}{1 - (\frac{P_2}{P_{t1w}})^{\frac{\gamma-1}{\gamma}}} \tag{12}$$

The only difference between the expressions of Eq. 10 and Eq. 12 is the denominator of the ideal process. In the latter efficiency definition, the main stream before the vane ($t1g$) and the

cooling supplied air ($t1ci$) are brought through a reversible adiabatic process in a common mixed state W (T_{tm}, P_{t1w}). As a result, the ideal expansion occurs from W to 2 final condition. Since the mixing process is assumed to be adiabatic, the stagnation temperature after mixing (T_{tm}) can be calculated from the steady flow energy equation, written for semi-perfect gases Eq. 13.

$$(1-\phi)\cdot\int_{T_{t1g}}^{T_{tm}} Cp_g(T)dT+\sum_{n=i}\phi_i\cdot\int_{T_{t1ci}}^{T_{tm}} Cp_g(T)dT=0 \quad (13)$$

In Eq. 13, ϕ_i is the mass flow ratio of each cooling tube ($\phi_i=\frac{m_{ci}}{m_g+\sum m_{ci}}$, $\phi=\sum\phi_{ci}$), while the summation is over the n^{th} coolant streams. The generated entropy per unit mass related with pressure is computed in Eq. 14.

$$\sigma_P=(1-\phi)R_g ln(\frac{P_{t1g}}{P_{t1w}})+\sum_{n=i}\phi_i R_c ln(\frac{P_{tci}}{P_{t1w}}) \quad (14)$$

The WP efficiency definition demands for $\sigma_P=0$, hence the stagnation pressure can be calculated in Eq. 15.

$$\frac{P_{t1w}}{P_{t1g}}=\prod_i(\frac{P_{t1ci}}{P_{t1g}})^{\phi_i R_i/R} \quad (15)$$

As a consequence, by combining the cycle average approach for the flow properties the cycle average weighted-pressure mixed efficiency can be deduced for the case of the flow control system. Additionally, the vane is evaluated in terms of pressure losses over oscillations also. The total pressure losses are calculated in accordance to Eq. 16.

$$\zeta_{P_t}=\frac{P_t{}_{Out}^{MA}-P_t{}_{In}^{MA}}{P_t{}_{In}^{MA}} \quad (16)$$

It is necessary to evaluate the effect of the flow control system in the distribution of the losses. For the purposes of the current study, the estimation of losses by Aungier [36] is introduced. The formula of the loss coefficients can be found in Appendix B. The scope of this work is the evaluation of a vane. As a result, the total pressure loss coefficient (Y) is split to the contribution of the profile losses (Y_p), the secondary losses (Y_s), the trailing edge losses (Y_{te}) and the shock losses (Y_{sh}). In addition, for the case of the flow control system the term of the mixing losses (Y_m) between the main stream and the secondary air supply system is introduced. For the specific case of Y_s, the coefficient cannot be calculated as the span of the vane is changing along the axis of the cascade. The correlation of secondary losses [36] demands a unique value of the vane span. As a result, the total pressure loss coefficient is firstly estimated and then Y_s is subtracted by calculating the other coefficients. The distribution of the losses is conducted after performing the cycle average process. Thus, for the case without the flow control the loss distribution analysis is given by Eq. 17, whereas when the flow control system is applied the distribution of losses is derived by Eq. 18, 19 and 20. For the latter case, the loss distribution of the vane takes place after splitting the domain into two parts. By introducing the stagnation pressure in the leading edge after the blowing tubes (01 at Fig. 8), the mixing loss coefficient can be computed.

$$Y=\frac{\overline{(P_t)}_1^{WA}-\overline{(P_t)}_2^{WA}}{\overline{(P_t)}_2^{WA}-\overline{(P)}_2^{AA}}\rightarrow Y=Y_p+Y_s+Y_{te}+Y_{sh} \quad (17)$$

$$Y=\frac{\overline{(P_t)}_w^{WA}-\overline{(P_t)}_2^{WA}}{\overline{(P_t)}_2^{WA}-\overline{(P)}_2^{AA}}\rightarrow \quad (18)$$

$$Y=\frac{\overline{(P_t)}_w^{WA}-\overline{(P_t)}_{01}^{WA}+\overline{(P_t)}_{01}^{WA}-\overline{(P_t)}_2^{WA}}{\overline{(P_t)}_2^{WA}-\overline{(P)}_2^{AA}}\rightarrow \quad (19)$$

$$Y=Y_m+Y_{Airfoil}\rightarrow Y=Y_m+Y_p+Y_s+Y_{te}+Y_{sh} \quad (20)$$

Concerning the oscillating behaviour of each component, the reduced range [37, 38] of the transient total pressure signals at inlet of domain and outlet of transition duct are calculated. Thus, the damping factor can be computed in Eq. 21.

$$\hat{R}=\frac{Range(P_t^{MA})}{\frac{1}{\tau}\int_0^\tau(P_t^{MA})\,dt}\rightarrow D_{\hat{R}}=\frac{\hat{R}_{In}-\hat{R}_{Out}}{\hat{R}_{Out}} \quad (21)$$

3.4 Results of Flow Control

In Fig. 10, the evolution of mass–weighted average stagnation pressure in various locations for the case without flow control at 0.5 kHz is portrayed. In the inlet of the vane, the signal of the pressure is highly oscillated. This emerges from the reflection of the pulsating wave by the leading edge. When the pulsation approaches the leading edge the wave is reflected upstream. As a result, the incoming pulsation meets the reflection and the stagnation pressure locally is excited. This phenomenon is predominant since the pulsation has a small amplitude.

In Fig. 11, the losses–oscillation analysis of the aforementioned example is presented for the eight cycle. In Fig. 11a and Fig. 11c, average losses and damping factors for each component are placed. The analysis is split into three parts: a) Inlet of Vane ($0\rightarrow 01$ of Fig.8), Diffusive Endwalls ($01\rightarrow 1$ of Fig.8) and Vane ($1\rightarrow 2$ of Fig.8). On the contrary, in Fig. 11b and Fig. 11d the cumulative evaluation is performed. Here, the inlet of the domain is directly compared with the outlet of each part. Concerning losses, the vane is responsible for the majority of them. For the damping factor, the inlet part of the vane excites significantly the signal due to the wave reflection, while the vane contributes with a very small level of excitation. Consequently, the cumulative excitation is connected with the inlet part and the wave reflection rather than the vane itself.

The analysis of Fig. 11 is conducted for every frequency and all the cases of Table 6. The results of this parametric analysis can be found in Fig. 12, where the reduced frequency is placed in x–abscissa and the vane damping factor in y–abscissa. Each case is coloured with the cycle average deviation coefficient of Eq. 11. The consideration of the cumulative evaluation indicates excitation for each frequency of all cases. Nonetheless, as it is

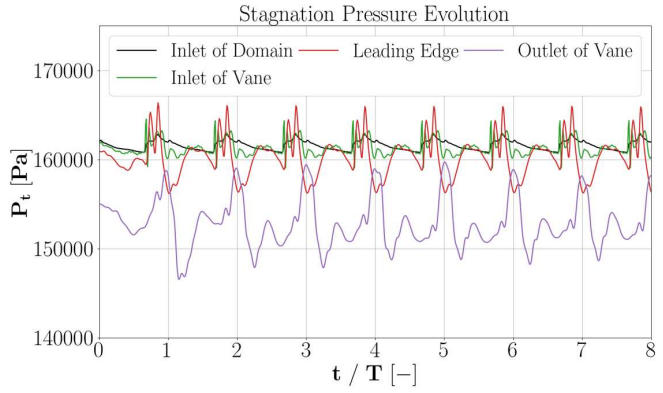

FIGURE 10: MASS WEIGHTED AVERAGE STAGNATION PRESSURE SIGNALS WITHOUT FLOW CONTROL AT $f = 0.5\ kHz$

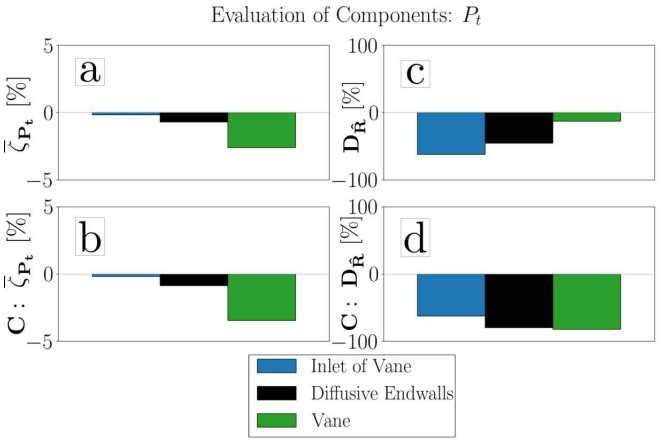

FIGURE 11: LOSSES - OSCILLATION ANALYSIS WITHOUT FLOW CONTROL AT $f = 0.5\ kHz$

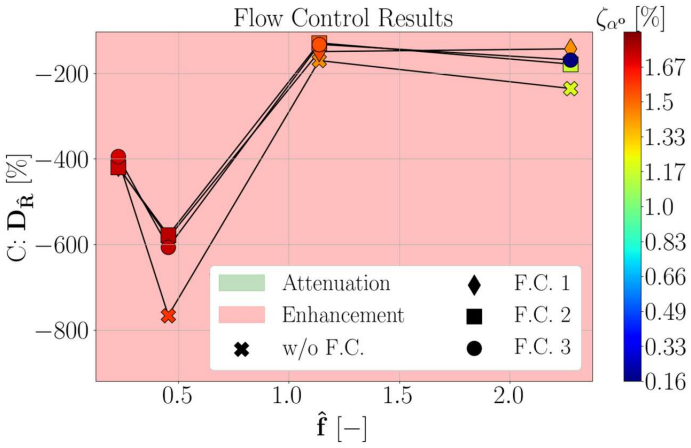

FIGURE 12: FLOW CONTROL RESULTS: CUMULATIVE EVALUATION

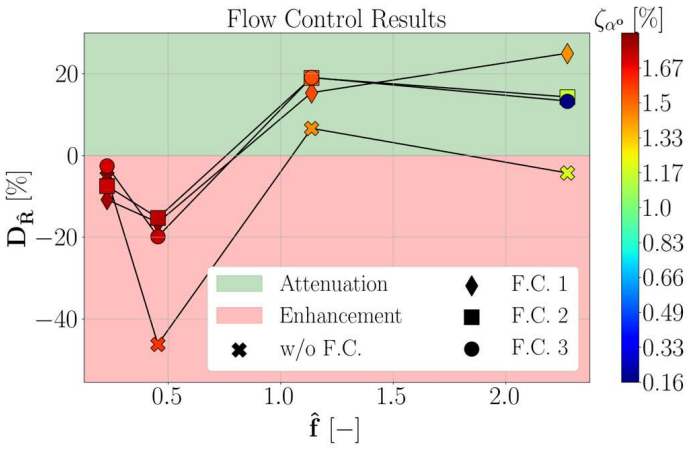

FIGURE 13: FLOW CONTROL RESULTS: COMPONENT EVALUATION

mentioned it must be distinguished the vane inlet part with the stator, as the reflection excites significantly the signals. As a result, the analysis of the flow control system should concentrate to Fig. 13, which provides the component evaluation. Table 9 enlists the cycle average blowing ratio between the main–flow and the flow control system for the three cases at 5 kHz. For the cases without flow control, the vane as a component attenuates the signal only at 2.5 kHz. On the contrary, if the reduced frequency exceeds the unity, the flow control offers attenuation for every case. In particular, at the highest frequency of 5 kHz the less the blowing pressure the better in terms of attenuation. The maximum attenuation of 25 % is observed for F.C.1 at 5 kHz. Moreover, for all the cases as the reduced frequency increases the deviation coefficient decreases. In fact, the F.C.3 at 5 kHz offers the best deviation flow coefficient preserving it below 1 %.

Concerning the stator's efficiency, Fig. 14, includes a parametric analysis of the flow control system for every frequency. For the case without the flow control system the cycle average efficiency of Eq. 10 is calculated. By increasing the frequency, the efficiency of the vane without the flow control increases. On the other hand, for the flow control cases the WP efficiency definition of Eq. 12 is used. All the cases exhibit larger efficiency with respect the flow control case except the 2.5 kHz and the F.C.1. of 5 kHz. The maximum efficiency of 0.918 is achieved for F.C.3 at 5 kHz.

In Fig. 15, the distribution of losses for the cascade can be seen for every frequency for the case with and without the flow control. The total pressure loss coefficient is increased for every frequency for the cases of flow control, due to mainly the addition of the mixing losses. The distribution of losses seems to be stable for each case and no major differences can be detected. In general, it seems that the contribution of secondary flow losses is increasing with more elevated blowing pressure. In fact, this

TABLE 9: CYCLE AVERAGE BLOWING RATIO FOR 5 [kHz]

Case	F.C.1	F.C.2	F.C.3
M	0.72 [−]	0.9092 [−]	0.9579 [−]

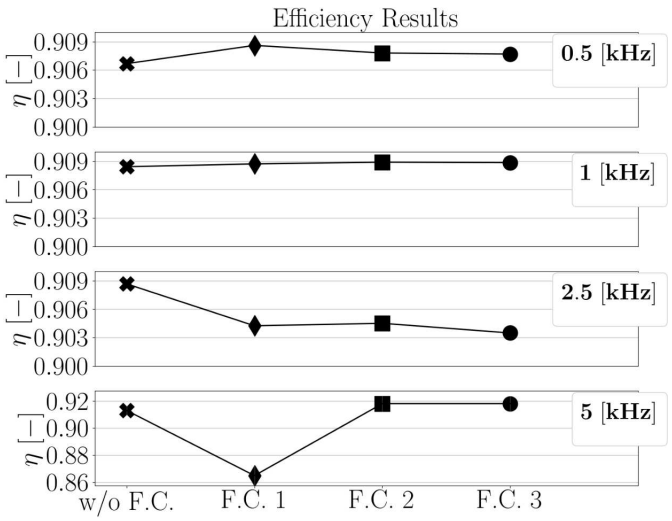

FIGURE 14: PARAMETRIC ANALYSIS OF EFFICIENCY

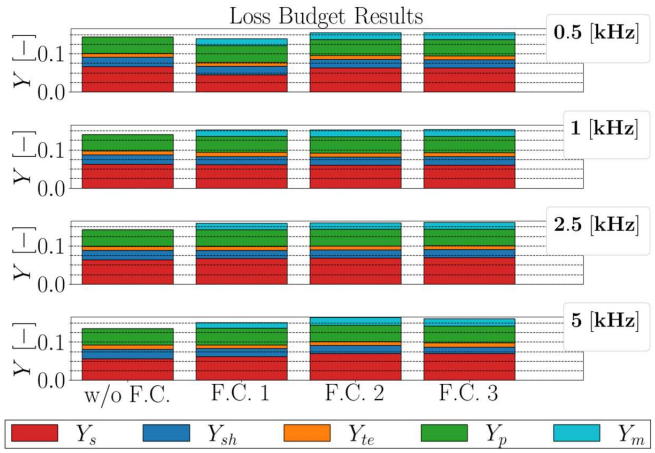

FIGURE 15: DISTRIBUTION OF LOSSES WITH AND WITHOUT FLOW CONTROL

argument can be identified for the case of 5 kHz.

In Fig. 16, a flow field comparison with the help of turbulent intensity is conducted at the outlet of the vane without and with flow control of F.C.3 at 5 kHz. The flow field is sampled at t_1 = 20 %, t_2 = 40 %, t_3 = 60 %, t_4 = 80 %, t_5 = 100 % of the last period of both cases. Starting by t_1, the passage vortices without flow control are affected more by the mild incoming pulsation approaching the trailing edge of the preceding vane. This is especially profound on t_2, when the hub passage vortex almost touches the trailing edge. In t_3, the pulsation approaches its minimum level and the passage vortices are guided towards hub and tip respectively. After the pulsation maximum point at t_4 the vortices are headed towards the midspan, while the flow control system keeps them close to the suction side. The case without the flow control cannot restrict the motion of the vortices and they approach the trailing edge of the preceding vane. On t_5, the flow control system achieves more concentrated passage vortices while

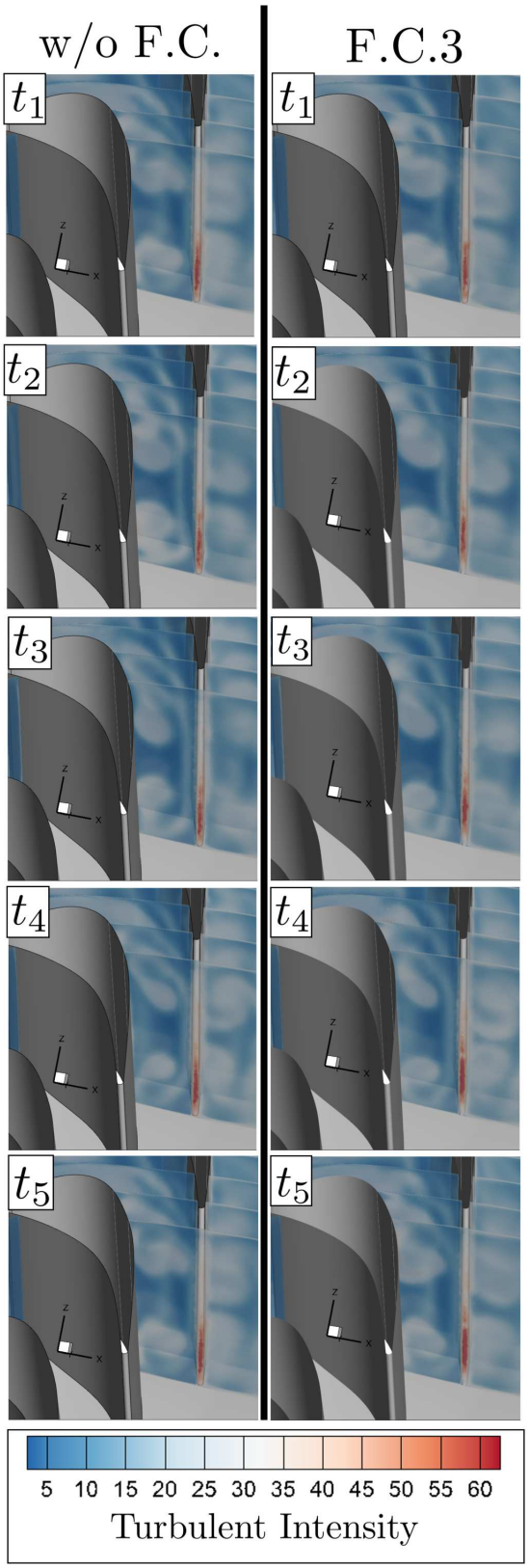

FIGURE 16: SECONDARY FLOWS EVOLUTION WITH AND WITHOUT FLOW CONTROL FOR 5 kHz at t_1 = 20%, t_2 = 40%, t_3 = 60%, t_4 = 80%, t_5 = 100% OF THE CYCLE

the case without the flow control results in almost split vortices at hub and tip respectively. In conclusion, the flow control system manages to restrict the motion of the passage vortices providing an outflow with higher efficiency, less deviation coefficient and vane attenuation at 5 kHz.

4. CONCLUSION

The current manuscript focuses on the design of a HPT vane to ingest the high enthalpy inflow of an RDE by numerical means. In addition, a flow control system is proposed and numerically analysed. The tip and hub endwalls upstream the leading edge of the CT3 vane and the airfoil profile are parametrized and a large DOE is numerically tested under steady inlet conditions. An optimization methodology provides the best geometry in terms of loss coefficient. A flow field comparison of the worst and best case uncovered that the restricted size of secondary flows for the best case decreases the losses and the deviation coefficient as well.

In the second part of the current study a flow control system is proposed. An array of cooling tubes are inserted in the diffusive endwalls of tip and hub upstream of the leading edge. A parametric CFD analysis under perturbing inlet conditions of the main flow for four different frequencies without and with the flow control system is taken place. In parallel, the activity attempts to investigate the influence of the steady supplying stagnation pressure of the flow control system. In general, the flow control system manages to attenuate, decrease the deviation coefficient and increase the efficiency for high frequency.

A flow field comparison of F.C.3 and the case without the flow control system at 5 kHz is performed. The flow control system restricts the motion of the tip and hub passage vortex under pulsating inflow. As a result, the vane attenuates the flow field, the efficiency is increased and the deviation coefficient experiences a reduction of 86 %. In conclusion, the flow control system restricts the oscillating inflow and guides better the outflow for the subsequent rotor. The next step of the activity will be the investigation of the flow control under spatio–temporal resolved inlet boundary conditions that are representative of RDE perturbing outflow. In addition, it will be analysed the integration of the CT3 rotor blade downstream of the optimized stator in order to numerically investigate the influence of the flow control system to the stage's performance.

ACKNOWLEDGMENTS

The present activity is performed in the frame of the INSPIRE project (Grant Agreement 956803) funded by the European Commission through a Marie Sklodowska-Curie action. We acknowledge the CINECA award under the ISCRA initiative, for the availability of high-performance computing resources and support. Moreover, computational resources were provided by HPC@POLITO. The authors are grateful to the TATEF2 consortium for the permission to use the CT3 experimental data generated at the von Karman Institute for Fluid Dynamics. The authors would like to thank Nicola Rosafio for his help to the validation and optimization part of this activity.

REFERENCES

[1] Perkins, H Douglas and Paxson, Daniel E. "Summary of pressure gain combustion research at NASA." Technical report no. NASA / TM-2018-219874. 2018.

[2] Glassman, Irvin, Yetter, Richard A. and Glumac, Nick G. "Flame phenomena in premixed combustible gases." *Combustion*, 5th ed. Academic Press, Waltham (2015): Chap. 4, pp. 147–254. DOI 10.1016/b978-0-12-407913-7.00004-9.

[3] Heiser, William H. and Pratt, David T. "Thermodynamic Cycle Analysis of Pulse Detonation Engines." *Journal of Propulsion and Power* Vol. 18 No. 1 (2002): p. 68–76. DOI 10.2514/2.5899.

[4] Stathopoulos, Panagiotis, Vinkeloe, Johann and Paschereit, Christian Oliver. "Thermodynamic evaluation of constant volume combustion for gas turbine power cycles." *Numerical Set Updings of the 11th International Gas Turbine Congress*: pp. 15–20. 2015. Tokyo, Japan.

[5] Hishida, Manabu, Fujiwara, Toshi and Wolanski, Piotr. "Fundamentals of rotating detonations." *Shock Waves* Vol. 19 No. 1 (2009): p. 1–10. DOI 10.1007/s00193-008-0178-2.

[6] Lu, Frank K. and Braun, Eric M. "Rotating Detonation Wave Propulsion: Experimental Challenges, Modeling, and Engine Concepts." *Journal of Propulsion and Power* Vol. 30 No. 5 (2014): p. 1125–1142. DOI 10.2514/1.b34802.

[7] Rankin, Brent A., Fotia, Matthew L., Naples, Andrew G., Stevens, Christopher A., Hoke, John L., Kaemming, Thomas A., Theuerkauf, Scott W. and Schauer, Frederick R. "Overview of Performance, Application, and Analysis of Rotating Detonation Engine Technologies." *Journal of Propulsion and Power* Vol. 33 No. 1 (2017): p. 131–143. DOI 10.2514/1.b36303.

[8] Sousa, Jorge, Paniagua, Guillermo and Collado Morata, Elena. "Thermodynamic analysis of a gas turbine engine with a rotating detonation combustor." *Applied Energy* Vol. 195 (June 2017): p. 247–256. DOI 10.1016/j.apenergy.2017.03.045.

[9] Schwer, Douglas and Kailasanath, Kailas. "Numerical Investigation of Rotating Detonation Engines." *46th AIAA/ASME/SAE/ASEE Joint Propulsion Conference amp;amp; Exhibit*. 2010. American Institute of Aeronautics and Astronautics. DOI 10.2514/6.2010-6880.

[10] Schwer, Douglas A., Brophy, Christopher M. and Kelso, Robert H. "Pressure Characteristics of an Aerospike Nozzle in a Rotating Detonation Engine." *2018 Joint Propulsion Conference*. 2018. American Institute of Aeronautics and Astronautics. DOI 10.2514/6.2018-4968.

[11] Liu, Z., Braun, J. and Paniagua, G. "Characterization of a Supersonic Turbine Downstream of a Rotating Detonation Combustor." *Journal of Engineering for Gas Turbines and Power* Vol. 141 No. 3 (2018). DOI 10.1115/1.4040815.

[12] Naples, Andrew, Hoke, John, Battelle, Ryan and Schauer, Fred. "T63 Turbine Response to Rotating Detonation Combustor Exhaust Flow." *Journal of Engineering for Gas Turbines and Power* Vol. 141 No. 2 (2019): p. 021029. DOI 10.1115/1.4041135.

[13] Zhou, Shengbing, Ma, Hu, Li, Shuai, Liu, Daokun, Yan, Yu and Zhou, Changsheng. "Effects of a turbine guide vane on hydrogen-air rotating detonation wave propagation characteristics." *International Journal of Hydrogen Energy* Vol. 42 No. 31 (2017): p. 20297–20305. DOI 10.1016/j.ijhydene.2017.06.115.

[14] Wei, Wan-li, Wu, Yu-wen, Weng, Chun-sheng and Zheng, Quan. "Influence of propagation direction on operation performance of rotating detonation combustor with turbine guide vane." *Defence Technology* Vol. 17 No. 5 (2021): p. 1617–1624. DOI 10.1016/j.dt.2020.08.009.

[15] Wu, Yuwen, Weng, Chunsheng, Zheng, Quan, Wei, Wanli and Bai, Qiaodong. "Experimental research on the performance of a rotating detonation combustor with a turbine guide vane." *Energy* Vol. 218 (2021): p. 119580. DOI 10.1016/j.energy.2020.119580.

[16] Bach, Eric, Paschereit, Christian Oliver, Stathopoulos, Panagiotis and Bohon, Myles D. "Rotating Detonation Wave Direction and the Influence of Nozzle Guide Vane Inclination." *AIAA Journal* Vol. 59 No. 12 (2021): p. 5276–5287. DOI 10.2514/1.j060594.

[17] Paniagua, G., Iorio, M.C., Vinha, N. and Sousa, J. "Design and analysis of pioneering high supersonic axial turbines." *International Journal of Mechanical Sciences* Vol. 89 (2014): p. 65–77. DOI 10.1016/j.ijmecsci.2014.08.014.

[18] Asli, Majid, Stathopoulos, Panagiotis and Paschereit, Christian Oliver. "Aerodynamic Investigation of Guide Vane Configurations Downstream a Rotating Detonation Combustor." *Journal of Engineering for Gas Turbines and Power* Vol. 143 No. 6 (2021). DOI 10.1115/1.4049188.

[19] Liu, Zhe, Braun, James and Paniagua, Guillermo. "Integration of a transonic high-pressure turbine with a rotating detonation combustor and a diffuser." *International Journal of Turbo amp; Jet-Engines* Vol. 40 No. 1 (2023): p. 1–10. DOI 10.1515/tjj-2020-0016.

[20] Liu, Zhe, Braun, James and Paniagua, Guillermo. "Performance of axial turbines exposed to large fluctuations." *53rd AIAA/SAE/ASEE Joint Propulsion Conference*. 2017. American Institute of Aeronautics and Astronautics. DOI 10.2514/6.2017-4817.

[21] Liu, Zhe, Braun, James and Paniagua, Guillermo. "Thermal power plant upgrade via a rotating detonation combustor and retrofitted turbine with optimized endwalls." *International Journal of Mechanical Sciences* Vol. 188 (2020): p. 105918. DOI 10.1016/j.ijmecsci.2020.105918.

[22] Grasa, Sergio and Paniagua, Guillermo. "Design, Multi-Point Optimization and Analysis of Diffusive Stator Vanes to Enable Turbine Integration Into Rotating Detonation Engines." *Turbo Expo: Power for Land, Sea, and Air*, Vol. 86984: p. V005T06A007. 2023. American Society of Mechanical Engineers. DOI https://doi.org/10.1115/GT2023-101726.

[23] Dénos, R, Sieverding, C. H., Arts, T, Brouckaert, J. F., Paniagua, G and Michelassi, V. "Experimental investigation of the unsteady rotor aerodynamics of a transonic turbine stage." *Proceedings of the Institution of Mechanical Engineers, Part A: Journal of Power and Energy* Vol. 213 No. 4 (1999): p. 327–338. DOI 10.1243/0957650991537653.

[24] Ayancik, Fatma, Acar, Erdem, Celebioglu, Kutay and Aradag, Selin. "Simulation-based design and optimization of Francis turbine runners by using multiple types of metamodels." *Proceedings of the Institution of Mechanical Engineers, Part C: Journal of Mechanical Engineering Science* Vol. 231 No. 8 (2016): p. 1427–1444. DOI 10.1177/0954406216658078.

[25] Roache, Patrick J. "Verification of Codes and Calculations." *AIAA Journal* Vol. 36 No. 5 (1998): p. 696–702. DOI 10.2514/2.457.

[26] Menter, F. R. "Two-equation eddy-viscosity turbulence models for engineering applications." *AIAA Journal* Vol. 32 No. 8 (1994): p. 1598–1605. DOI 10.2514/3.12149.

[27] Gallis, Panagiotis, Misul, Danieal Anna, Bellenoue, Marc, Boust, Bastien and Salvadori, Simone. "Development of 1D Model of Constant-Volume Combustor and Numerical Analysis of the Exhaust Nozzle." *Energies* Vol. 17 No. 5 (2024): p. 1191. DOI https://doi.org/10.3390/en17051191.

[28] Schwer, Douglas and Kailasanath, Kailas. "Numerical Investigation of Rotating Detonation Engines." *46th AIAA/ASME/SAE/ASEE Joint Propulsion Conference amp;amp; Exhibit*. 2010. American Institute of Aeronautics and Astronautics. DOI 10.2514/6.2010-6880.

[29] Schwer, Douglas A., Brophy, Christopher M. and Kelso, Robert H. "Pressure Characteristics of an Aerospike Nozzle in a Rotating Detonation Engine." *2018 Joint Propulsion Conference*. 2018. American Institute of Aeronautics and Astronautics. DOI 10.2514/6.2018-4968.

[30] Liu, Z., Braun, J. and Paniagua, G. "Characterization of a Supersonic Turbine Downstream of a Rotating Detonation Combustor." *Journal of Engineering for Gas Turbines and Power* Vol. 141 No. 3 (2018). DOI 10.1115/1.4040815.

[31] Cumpsty, N. A. and Horlock, J. H. "Averaging Nonuniform Flow for a Purpose." *Journal of Turbomachinery* Vol. 128 No. 1 (2005): p. 120–129. DOI 10.1115/1.2098807.

[32] George, A. St., Driscoll, R., Gutmark, E. and Munday, D. "Experimental Comparison of Axial Turbine Performance Under Steady and Pulsating Flows." *Journal of Turbomachinery* Vol. 136 No. 11 (2014): p. 111005. DOI 10.1115/1.4028115.

[33] Xisto, Carlos, Petit, Olivier, Gr¨onstedt, Tomas, Rolt, Andrew, Lundbladh, Anders and Paniagua, Guillermo. "The efficiency of a pulsed detonation combustor–axial turbine integration." *Aerospace Science and Technology* Vol. 82–83 (2018): p. 80–91. DOI 10.1016/j.ast.2018.08.038.

[34] Suresh, Ambady, Hofer, Douglas C. and Tangirala, Venkat E. "Turbine Efficiency for Unsteady, Periodic Flows." *Journal of Turbomachinery* Vol. 134 No. 3 (2011). DOI 10.1115/1.4003246.

[35] Young, J. B. and Horlock, J. H. "Defining the Efficiency of a Cooled Turbine." *Journal of Turbomachinery* Vol. 128 No. 4 (2006): p. 658–667. DOI 10.1115/1.2218890.

[36] Aungier, Ronald H. *Turbine Aerodynamics: Axial-Flow and Radial-Flow Turbine Design and Analysis*. ASME Press,

New York (2006): Chap. 4, pp. 61–91. URL http://dx.doi.org/10.1115/1.802418.

[37] Liu, Zhe, Braun, James and Paniagua, Guillermo. "Integration of a transonic high-pressure turbine with a rotating detonation combustor and a diffuser." *International Journal of Turbo amp; Jet-Engines* Vol. 0 No. 0 (2020). DOI 10.1515/tjeng-2020-0016.

[38] Liu, Zhe, Braun, James and Paniagua, Guillermo. "Performance of axial turbines exposed to large fluctuations." *53rd AIAA/SAE/ASEE Joint Propulsion Conference*. 2017. American Institute of Aeronautics and Astronautics. DOI 10.2514/6.2017-4817.

[39] Paniagua, G., Dénos, R. and Almeida, S. "Effect of the Hub Endwall Cavity Flow on the Flow-Field of a Transonic High-Pressure Turbine." *Journal of Turbomachinery* Vol. 126 No. 4 (2004): p. 578–586. DOI 10.1115/1.1791644.

[40] Dénos, R., Arts, T., Paniagua, G., Michelassi, V. and Martelli, F. "Investigation of the Unsteady Rotor Aerodynamics in a Transonic Turbine Stage." *Journal of Turbomachinery* Vol. 123 No. 1 (2000): p. 81–89. DOI 10.1115/1.1314607.

APPENDIX A. VALIDATION OF ANSYS CFX SOLVER

The CFX ANSYS solver is validated with the help of the experimental data of the CT3 stage [39, 40].The performance of the stage is evaluated with RANS calculations and the interface between stator and rotor is modelled as mixing plane. The domain of $8.3 \cdot 10^6$ elements can be seen in Fig. 17. In addition, the boundary conditions of the domain are placed in Table 10. A pressure-based implicit coupled solver, is used for this analysis. A high-resolution scheme is selected for the advection terms and the turbulence, while the k–ω SST model [26] is used for modelling the turbulence. In addition, the inflation layer close to the walls ensures that the y^+ is maintained below 1. The working fluid is air, which is assumed to be ideal gas. The cavity between the stator and the rotor platform is included by specifying an outlet boundary condition. The cavity mass flow is elected −0.5 % of the main–flow in order to correspond with the available experimental data. The rotor speed is 6500 rpm, while heat transfer is allowed between the fluid medium and the walls.

Boundary Conditions	
Type	Properties
Inlet	$P_t = 161600\ [Pa]$ & $T_t = 440\ [K]$
Outlet	$P = 53333.3\ [Pa]$
Periodic	-
Mixing Plane	-
No–Slip Wall	$T_{wall} = 310\ [K]$

TABLE 10: BOUNDARY CONDITIONS OF CT3 STAGE

In Fig. 18, the non–dimensional pressure distribution in the 15 % and 50 % of the CT3 vane span is given for the experimental campaign and the numerical simulation. It is evident that ANSYS CFX Solver is able to produce the same distribution with the experiments. In the aft part of the vane, the numerical results slightly mismatch the experiments, as the cavity at the hub is not properly simulated. The gap of the hub between the stator and rotor platform affects the pressure in the hub region at the outlet of the vane. As a result, the mismatch at 50 % of span can be justified by the specification of the cavity as outlet boundary condition. In addition, the phenomena inside the passage are unsteady, in spite of the steady inlet boundary conditions. Overall, the solver achieved to reproduce the experimental data within an acceptable range. Thus, the solver can be used for the optimization of the High–Pressure Turbine vane with diffusive endwalls of Section 2.

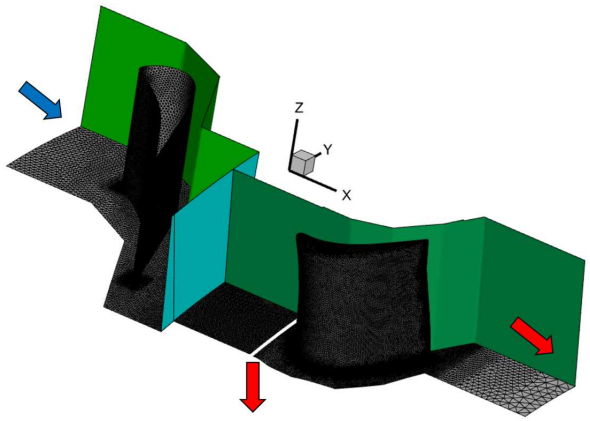

FIGURE 17: MESHED VOLUME OF CT3 STAGE

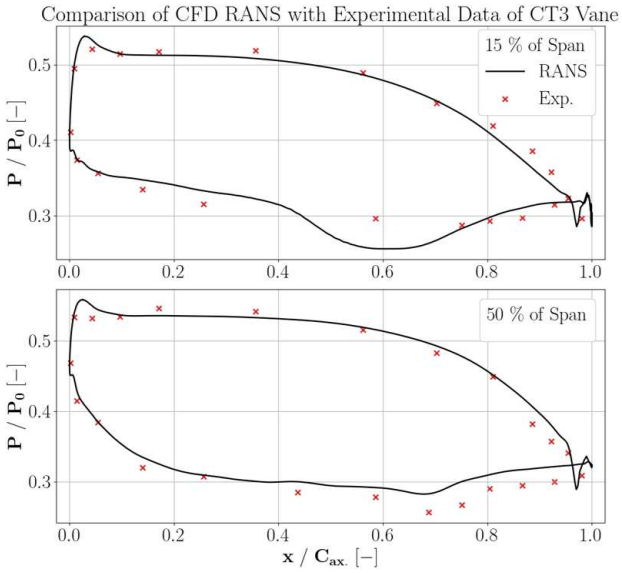

FIGURE 18: VALIDATION OF ANSYS CFX SOLVER FOR CT3 STAGE

APPENDIX B. LOSS BUDGET ANALYSIS

The total pressure loss coefficient analysis is based on the empirical performance models of axial–flow turbine blade/vane rows. These models are retrieved by the work of Aungier [36]. The total pressure loss coefficient is expressed as a summation of the source loss of a turbine. The division of losses is given by Eq. 22. In the current study, a transonic vane is investigated. Consequently, the losses arose by leakage, supersonic expansion and lashing wire are considered zero ($Y_{cl} = Y_{ex} = Y_{lw} = 0$). The utilized coefficients can be found in Table 11. Profile loss coefficient (Y_p) includes the losses arose by the boundary layer of the endwalls and the airfoil as well as the incidence failure of the cascade. On the other hand, Secondary Flow loss coefficient (Y_s) accounts for the losses derived by the effect of the centrifugal forces in the flow field. The Trailing Edge term (Y_{te}) is referred to the losses by the wake of the cascade, while the Shock losses (Y_{sh}) accounts for the compressibility effects through the cascade. The definition of the additional variables and terms of Table 11 to compute each loss coefficient can be found in [36].

$$Y = Y_p + Y_s + Y_{te} + Y_{cl} + Y_{ex} + Y_{sh} + Y_{lw} \tag{22}$$

Profile Losses	$Y_p = K_{mod}K_{inc}K_M K_M K_P K_{RE} A$ $A = [Y_{p1} + \Xi(Y_{p2} - Y_{p1})](5t_{max} \,/\, c)^{\Xi} - \Delta Y_{te}$ $\Xi = \alpha_{2,\,metal} \,/\, \alpha_2$
Trailing Edge Losses	$Y_{te} = [t_2 \,/\, (s \cdot sin\alpha_g - t_2)]^2$ $\alpha_g = arcsin(o \,/\, s)$
Shock Losses	$Y_{sh} = \sqrt{\tilde{Y}_{sh}^2 \,/\, (1 + \tilde{Y}_{sh}^2)}$ $\tilde{Y}_{sh} = 0.8 \cdot X_1^2 + X_2^2$ $X_1 = 0$, if $Ma_1 \leq 0.4$ $X_1 = Ma_1 - 0.4$, if $Ma_1 > 0.4$ $X_2 = 0$, if $Ma_1 \leq Ma_2$ $X_2 = Ma_1 \,/\, Ma_2 - 1$, if $Ma_1 > Ma_2$

TABLE 11: LOSS COEFFICIENTS OF A VANE

APPENDIX C. OPTIMIZED GEOMETRY

The non-dimensional geometrical data of the optimized vane can be found in the Tables 12, 13 and 14.

Point	$z \,/\, C$	$y \,/\, C$
1	0.2052	4.9987
2	0.2443	4.999
3	0.2833	4.9999
4	0.3224	5.0016
5	0.3614	5.0041
6	0.4003	5.0077
7	0.4391	5.0125
8	0.4777	5.019
9	0.5158	5.0274
10	0.5533	5.0383
11	0.5899	5.0523
12	0.625	5.0694
13	0.659	5.0886
14	0.6934	5.1073
15	0.7285	5.1244
16	0.7645	5.1396
17	0.8013	5.1527
18	0.8236	5.1594
19	0.8545	5.1675
20	0.8856	5.1742
21	0.9171	5.1798
22	0.9486	5.1844
23	0.9803	5.1884
24	1.012	5.1918
25	1.0438	5.1948
26	1.0756	5.1976
27	1.1074	5.2002
28	1.1392	5.2026
29	1.171	5.205
30	1.2028	5.2072
31	1.2347	5.2094
32	1.2665	5.2115
33	1.2984	5.2135
34	1.3302	5.2154
35	1.3666	5.2175
36	1.4165	5.2199

TABLE 12: COORDINATES OF UPPER ENDWALL SPLINE

Point	z / C	x / C
1	0.6791	0.0298
2	0.6793	0.0334
3	0.6798	0.037
4	0.6805	0.0406
5	0.6814	0.0441
6	0.6825	0.0476
7	0.6838	0.051
8	0.6853	0.0543
9	0.7074	0.0946
10	0.7357	0.126
11	0.7703	0.1502
12	0.8093	0.1668
13	0.8508	0.1753
14	0.8931	0.1756
15	0.9345	0.1672
16	0.973	0.1496
17	1.0072	0.1246
18	1.0373	0.0948
19	1.0642	0.0621
20	1.0891	0.0277
21	1.1125	−0.0076
22	1.1351	−0.0435
23	1.1563	−0.0802
24	1.1756	−0.1179
25	1.1931	−0.1565
26	1.2091	−0.1957
27	1.2242	−0.2354
28	1.2384	−0.2753
29	1.2521	−0.3154
30	1.2653	−0.3557
31	1.2782	−0.3961
32	1.2907	−0.4366
33	1.3029	−0.4772
34	1.3149	−0.5179
35	1.3267	−0.5586
36	1.3383	−0.5993
37	1.3498	−0.6402
38	1.3562	−0.6933
39	1.3577	−0.6923
40	1.359	−0.691
41	1.3601	−0.6896
42	1.3609	−0.688
43	1.3614	−0.6863
44	1.3616	−0.6827
45	1.3617	−0.6845

TABLE 13: COORDINATES OF SUCTION SIDE

Point	z / C	x / C
1	0.6796	0.0213
2	0.6806	0.0164
3	0.6821	0.0117
4	0.6841	0.0072
5	0.6867	0.003
6	0.6897	−0.0009
7	0.6931	−0.0044
8	0.697	−0.0075
9	0.7274	−0.0269
10	0.754	−0.0432
11	0.7809	−0.0589
12	0.8081	−0.0743
13	0.8355	−0.0892
14	0.863	−0.1038
15	0.8907	−0.1182
16	0.9183	−0.1326
17	0.9459	−0.1472
18	0.9732	−0.1622
19	1.0002	−0.178
20	1.0265	−0.1946
21	1.052	−0.2127
22	1.0763	−0.2322
23	1.0993	−0.2532
24	1.1209	−0.2757
25	1.141	−0.2995
26	1.1599	−0.3244
27	1.1775	−0.3501
28	1.194	−0.3766
29	1.2096	−0.4036
30	1.2244	−0.431
31	1.2386	−0.4588
32	1.2523	−0.4868
33	1.2656	−0.515
34	1.2785	−0.5434
35	1.2912	−0.5719
36	1.3037	−0.6004
37	1.3161	−0.6291
38	1.3411	−0.6884
39	1.3421	−0.6901
40	1.3434	−0.6917
41	1.345	−0.6929
42	1.3467	−0.6939
43	1.3487	−0.6945
44	1.3507	−0.6947
45	1.3527	−0.6946

TABLE 14: COORDINATES OF PRESSURE SIDE